

A Parameterized Nonlinear Magnetic Equivalent Circuit for Design and Fast Analysis of Radial Flux Magnetic Gears with Bridges

Danial Kazemikia, Matthew C. Gardner, *Member, IEEE*
Department of Electrical Engineering, University of Texas at Dallas, Richardson, Texas

Magnetic gears offer significant advantages over mechanical gears, including contactless power transfer, but require efficient and accurate modeling tools for optimization and commercialization. This paper presents the first fast and accurate 2D nonlinear magnetic equivalent circuit (MEC) model for radial flux magnetic gears (RFMG), capable of analyzing designs with bridges—critical structural elements that introduce intense localized magnetic saturation. The proposed model systematically incorporates nonlinear effects while maintaining rapid simulation times through a parameterized geometry and adaptable flux tube distribution. A robust initialization strategy ensures reliable performance across diverse designs. Extensive validation against nonlinear finite element analysis (FEA) confirms the model’s accuracy in torque and flux density predictions. A comprehensive parametric study of 140,000 designs demonstrates close agreement with FEA results, with simulations running up to 100 times faster. Unlike previous MEC approaches, this model provides a generalized, computationally efficient solution for analyzing a wide range of RFMG designs with or without bridges, making it particularly well-suited for large-scale design optimization.

Index Terms—Design optimization, finite element analysis, magnetic equivalent circuit, magnetic gear, magnetic saturation, mesh-flux analysis, Newton-Raphson, nonlinear permeability, permeance network, radial flux, reluctance network

I. INTRODUCTION

MAGNETIC gears (MGs) represent an advanced power transmission technology that employs magnetic fields to facilitate the conversion between high-speed, low-torque and low-speed, high-torque mechanical rotation. Unlike conventional mechanical gear systems, MGs operate without physical contact, thereby providing inherent overload protection and reducing maintenance requirements. The contactless operation inherently isolates input and output shafts, enhancing system reliability while minimizing operational noise [1]. MGs offer promising solutions for robust and efficient energy transmission, with proposed applications including wind [2]–[4] and wave energy harvesting [5], traction applications [6], [7] such as electric vehicles [8]–[10], and aircraft propulsion [11]–[13]. The technology’s potential is further validated by NASA’s ongoing research into magnetic gearing for electric aviation applications [14]–[17].

Among MG topologies, radial flux MGs (RFMGs) are the most prevalent, offering the highest reported experimental torque densities [18]–[20]. As shown in Fig. 1, RFMGs consist of three concentric rotors: two permanent magnet (PM) rotors and magnetically permeable modulators positioned between them.

To fully unlock the potential of RFMGs and make them competitive with their mechanical counterparts in terms of size, weight, and cost, accurate and effective analysis tools are essential. While finite element analysis (FEA) is most commonly used for its accuracy and robustness in capturing complex nonlinear effects in complex geometries, it suffers from high computational costs that significantly increase simulation times for intricate designs such as RFMGs with

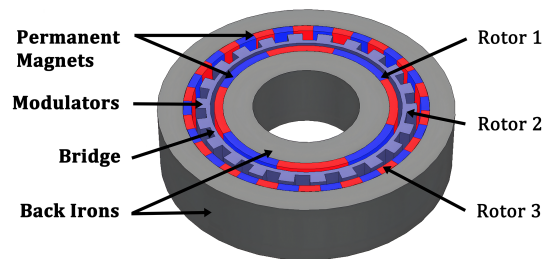


Fig. 1: Coaxial radial flux magnetic gear with surface-mounted PMs.

bridges [21], [22]. Analytical models and winding function theory (WFT) enable faster computation but tend to be less flexible and less accurate, particularly in representing complex flux paths and nonlinearities [23], [24]. However, magnetic equivalent circuit (MEC) models, also known as reluctance networks, balance accuracy and speed, making them suitable for optimization studies [21], [22].

While nonlinear MEC modeling is an established technique, none of the current implementations have addressed the inclusion of bridges in magnetic gears [25], [26]. Bridges are critical components in many practical RFMG designs, simplifying manufacturing and providing structural support to stabilize the modulators against the strong magnetic forces generated between the two sets of PMs [1], [3], [4], [7], [10], [20], [27]–[32]. Due to their position and thin structure, bridges experience highly localized and intense saturation, which, if not modeled accurately, can lead to significant errors. For instance, Fig. 2 shows Base Design 2 (detailed in Section III), a 2D magnetic gear design with bridges, experiencing significant saturation in portions of the bridges. In this case, linear and nonlinear FEA predict slip torques of 250.9 Nm

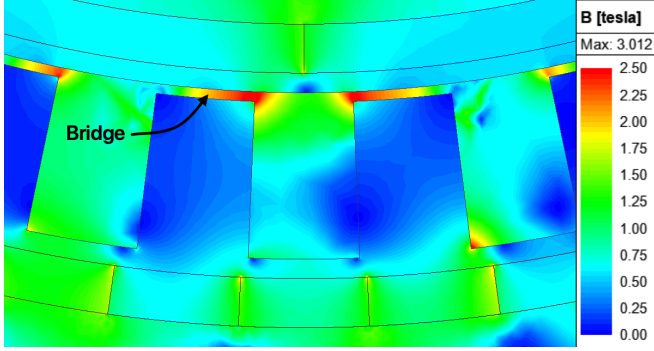


Fig. 2: Flux density (B) based on nonlinear FEA in an RFMG with bridges (Base Design 2)

and 13.5 kNm, respectively, a 92% discrepancy. Because the linear model does not account for saturation, it significantly overpredicts the leakage flux in the bridge. However, for the same design without bridges, linear and nonlinear FEA predict slip torques of 14.1 kNm and 14.4 kNm, respectively, only a 2% discrepancy. This stark contrast highlights the necessity of nonlinear modeling for designs with bridges, while linear models are sufficiently accurate for designs without bridges. Thus, it is necessary to develop a nonlinear MEC model capable of accurately modeling the effects of intense, localized saturation, as shown in Fig. 2.

Moreover, previous studies have focused on developing MEC models for specific magnetic gear designs without bridges rather than a general solution applicable to diverse RFMGs, with or without bridges. For example, [25], [26], [33], considered nonlinear effects but, in addition to not considering designs with bridges, lacked parameterized modeling and any explanation of robust systematic initialization methods, limiting their suitability for diverse designs. Comprehensive modeling capabilities are crucial for optimization studies, in which exploration of extensive design spaces is required.

Systematic discretization addresses this limitation by enabling seamless adaptation of the model to various geometries while maintaining precision and speed. Additionally, systematic initialization ensures consistent convergence across all designs. Newton-Raphson method is commonly employed for solving nonlinear models, but it is highly sensitive to the initial guess [34]. Without a reliable initialization strategy, the method may converge successfully for some designs while failing for others, making it unsuitable for design optimization.

To address these gaps, this paper presents a robust and adaptable nonlinear MEC model for RFMGs with bridges. The model incorporates systematic discretization and a reliable initialization strategy, ensuring consistent accuracy and convergence across a wide design space. This eliminates the need for manual re-meshing, tuning, or initialization for each different design. Benchmarking against FEA simulations confirms the model's accuracy and reliability across diverse RFMG designs, exceeding the scope of previous studies. To the authors' knowledge, this is the first nonlinear MEC capable of accurately modeling the designs with bridges and of consistently modeling such a broad range of magnetic gear

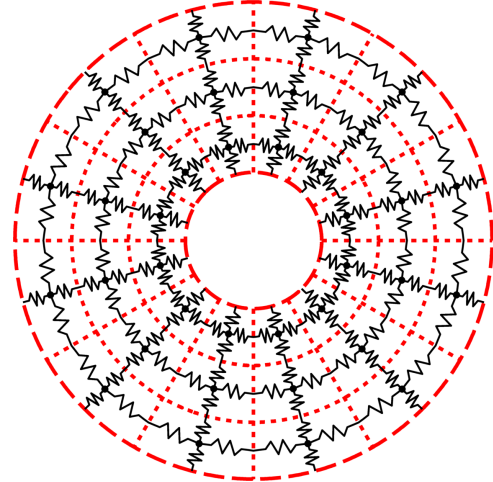


Fig. 3: Radial and angular layers and mesh node cells in a simple MEC example

designs.

II. IMPLEMENTATION

A. Meshing and the Node Cell

By discretizing (meshing) the MG into radial and angular (tangential) layers, the systematic, parameterized 2D MEC implemented in [21] and [35] is utilized. Fig. 3 shows an example of a source-free MEC, which consists of 3 radial layers, and 12 tangential layers. The dotted lines denote the boundaries of these layers. The overlap of each radial layer with each angular layer defines an arc-shaped region called a 2D node cell. As depicted in Fig. 3 each 2D node cell has four reluctances, two oriented radially and two oriented tangentially. These reluctances represent flux tubes that connect each node cell's boundary to the node cell's center, allowing positive or negative flux to flow from the center of the node cell to each of its boundaries.

If a flux tube contains a PM magnetized in the direction of the flux tube, an MMF source is placed in series with the reluctance. (In this paper, MMF sources only appear in the flux tubes oriented radially within the PMs since only radially magnetized PMs are considered.) These flux tubes are represented using the equivalent circuit configuration depicted in Fig. 4, in which \mathcal{R}_{rad} denotes the reluctance of the radial flux tube with the permeability of μ_{PM} , \mathcal{F}_{inj} signifies the equivalent magnetomotive force (MMF) injected by the PM, \mathcal{F}_{PM} represents the MMF drop across the flux tube, and Φ_{PM} indicates the magnetic flux in the flux tube.

In this study, as in [21], the MEC mesh is distributed throughout the geometry as illustrated in Fig. 5, depicting a very coarse mesh overlaid on the unrolled representation of an RFMG with $P_1 = 1$, $P_3 = 2$, and $Q_2 = 3$. This mesh distribution divides the geometry into an equal number of angular layers. It partitions the RFMG into eight distinct radial regions, the inner back iron, inner PMs, inner air gap, bridge, modulators, outer air gap, outer PMs, and the outer back iron. The meshing also extends to the air inside the inner back iron and outside the outer back iron. Each of these ten radial

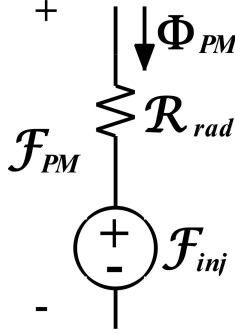


Fig. 4: Equivalent circuit representation of a radially oriented permanent magnet flux tube

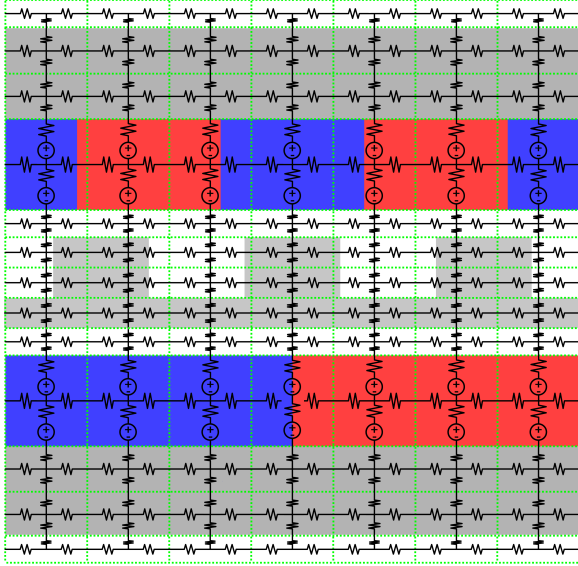


Fig. 5: MEC overlaid on an example unrolled RFGM

regions consists of several radial layers. The user determines the number of radial layers in each region and the number of angular layers based on the tradeoff between analysis speed and accuracy.

B. The System of Nonlinear Equations

The MEC model is developed based on mesh-flux analysis, derived from Ampere's circuital law, where the circulating magnetic fluxes in each mesh loop represent an independent unknown variable. Mesh-flux analysis is utilized like Kirchhoff's voltage law is employed in the mesh-current analysis of electrical circuits. As an example, Fig. 6 depicts a mesh loop of the MEC, featuring node cells in the PMs. Loops outside the PMs are modeled similarly, except they lack the MMF sources. Applying Ampere's law to the mesh loop in Fig. 6, results in a mesh-flux equation of the form

$$\sum_{i=1}^4 \mathcal{R}_i(\Phi) (\Phi_x - \Phi_i) = f_{inj,4} - f_{inj,2} \quad (1)$$

where the left-hand term represents the sum of the reluctances within the mesh multiplied by their respective fluxes. This term characterizes the MMF drop caused by the reluctances in the

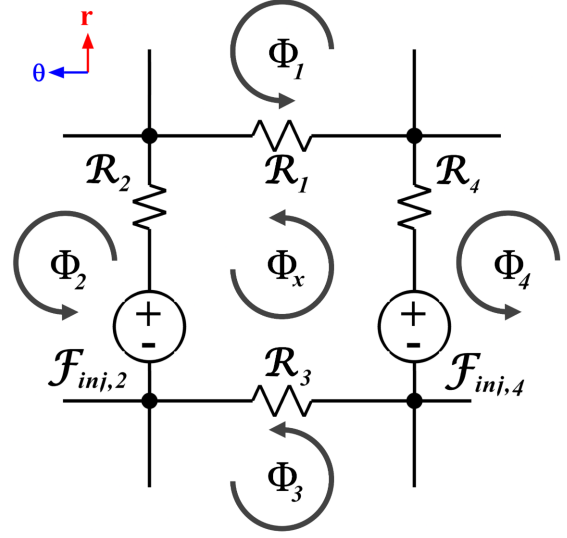


Fig. 6: 2D mesh loop schematic

loop and equals the sum of the injected MMF sources in that loop. In mesh-flux analysis, reluctances are utilized instead of permeances for ease of calculation. The reluctance of each flux tube is computed similarly to [21], except that, to represent saturation in ferromagnetic materials, the permeability depends on the flux density within the node cell.

The system of nonlinear equations describing the 2D MEC model is achieved by representing every mesh loop in the MEC by a mesh flux equation of the same basic form shown in (1). If the MEC consists of N_{AL} number of angular layers and N_{RL} number of radial layers, the number of mesh loops N equals $N_{AL} \times (N_{RL} - 1)$. This MEC model can be expressed in the matrix form as

$$[\mathcal{R}(\Phi)]_{N \times N} [\Phi]_{N \times 1} = [f]_{N \times 1} \quad (2)$$

where \mathcal{R} is the reluctance matrix, Φ is the column vector of unknown mesh fluxes, and f is the column vector of the algebraic sum of the MMFs injected by PMs in each loop.

In the reluctance matrix, \mathcal{R} , the i^{th} row corresponds to the i^{th} mesh loop in the MEC and contains the reluctance coefficients for that loop's flux equation, such as those shown on the left side of (1). The j^{th} column in \mathcal{R} corresponds to the j^{th} loop flux in the MEC. Entry $\mathcal{R}_{(i,j)}$ in \mathcal{R} contains the reluctance coefficient which describes the impact of the j^{th} loop's flux on the net MMF drop around the i^{th} loop. Each diagonal entry $\mathcal{R}_{(i,i)}$ in \mathcal{R} contains the positive sum of all reluctances surrounding the i^{th} loop. The reluctance coefficient of Φ_x in (1) illustrates a diagonal entry within the matrix representation of the system of equations, indicating the impact of the corresponding loop's flux on the net MMF drop around the loop. Each off-diagonal entry $\mathcal{R}_{(i,j)}$ (where $i \neq j$) in \mathcal{R} contains the negative value of the reluctance through which both the i^{th} and j^{th} loop fluxes pass. If those loops are not adjacent, the corresponding entry in \mathcal{R} is zero. The reluctance coefficients \mathcal{R}_1 , \mathcal{R}_2 , \mathcal{R}_3 , and \mathcal{R}_4 in (1) exemplify off-diagonal entries in the matrix form of the system of equations. Since all the reluctances in the MEC

are bidirectional, the matrix \mathcal{R} is always symmetric. Also, each loop in the MEC has four adjacent loops, except for the innermost and outermost loops, which lack adjacent loops on their radial inside and outside, respectively. As a result, all the rows in \mathcal{R} have five non-zero entries: one for each adjacent loop, as well as the diagonal entry in that row, except for the rows corresponding to the innermost and outermost loops, which have four non-zero entries. If the model exhibits symmetry, the analysis can be simplified by solving only the subset of equations corresponding to the mesh loops within a symmetrical fraction of the model.

Mesh-flux analysis was chosen over the node-MMF analysis used in [21], [35] due to a convergence issue encountered when solving the system of nonlinear equations with the Newton-Raphson method. Mesh-flux analysis directly outputs flux, from which flux density can easily be calculated to update permeability. On the other hand, node-MMF analysis calculates MMF; then, the reluctances, which depend on flux density, must be used to determine magnetic flux. However, this requires the use of reluctances from the previous iteration and can prevent convergence in many cases.

C. Nonlinear Analysis with Newton-Raphson Method

The 2D MEC model is analyzed by solving the following system of nonlinear equations, which can be rewritten from (2) as

$$\mathcal{R}(\Phi) \times \Phi - f = 0 \quad (3)$$

This nonlinear equation is solved iteratively using the Newton-Raphson method, as it generally offers relatively fast convergence [34]. At each iteration, by substituting the calculated Φ for the k^{th} iteration back into the left-hand side of (3) and updating the reluctances in \mathcal{R} yields the residual matrix, $r(\Phi)$, as in

$$\mathcal{R}(\Phi_k) \times \Phi_k - f = r(\Phi_k) \quad (4)$$

By applying Newton's method to (4), (5) is derived which is used to iteratively refine flux vector (Φ_k) to minimize the residuals error.

$$\Phi_{k+1} = \Phi_k - \frac{r(\Phi_k)}{r'(\Phi_k)} \quad (5)$$

Here, $r'(\Phi)$ is the Jacobian of $r(\Phi)$, which contains the partial derivatives of this multivariate function with respect to the mesh fluxes. The Jacobian matrix elements is shown to be calculated similarly to the reluctance matrix, $\mathcal{R}(\Phi)$, but using differential permeability instead of apparent permeability [36]. Therefore, (5) can be rewritten as

$$\Phi_{k+1} = \Phi_k - \frac{\mathcal{R}_{App}(\Phi_k) \times \Phi_k - f}{\mathcal{R}_{Diff}(\Phi_k)} \quad (6)$$

Here, $\mathcal{R}_{App}(\Phi_k)$ and $\mathcal{R}_{Diff}(\Phi_k)$ signify the reluctance matrix calculated using the apparent and differential permeabilities, respectively. After each iteration, the calculated mesh fluxes are used to compute flux density within each flux tube, which is then utilized to calculate the torque using Maxwell's stress

TABLE I: Magnetic gear base designs specifications

Parameter	Description	Base			Units
		Design 1	Design 2	Design 3	
P_1	Rotor 1 pole pairs	11	4	6	
P_3	Rotor 3 pole pairs	45	34	98	
r_o	Active outer radius	150	175	200	mm
T_{BI1}	Rotor 1 back iron thickness	20	35	40	mm
T_{PM1}	Rotor 1 PM thickness	9	5	13	mm
T_{AG1}	Inner air gap thickness	.5	2	1	mm
T_{Mods}	Rotor 2 thickness	11	17	14	mm
T_{Brg}	Bridge thickness	.5	1	1.5	mm
T_{AG2}	Outer air gap thickness	.5	2	1	mm
T_{PM3}	Rotor 3 PM thickness	7	5	7	mm
T_{BI3}	Rotor 3 back iron thickness	20	30	25	mm

tensor [21]. The flux densities are then used to update the permeabilities of the ferromagnetic node cells based on the B-H curve to recalculate \mathcal{R}_{App} and \mathcal{R}_{Diff} for the next iteration of (6).

The transformation of the Jacobian calculation into a form using differential permeability significantly reduces computational complexity. Traditional methods require calculating $N \times N$ partial derivatives for N mesh loops, with each derivative involving chain rule applications for the nonlinear B-H relationship [37]–[39]. This approach, however, simply recalculates the reluctance matrix using differential permeability, maintaining the same matrix structure and calculation methods. This reduces both computational cost and memory requirements while preserving accuracy in nonlinear magnetic systems. Moreover, the matrix factorization method, proposed in [40] is utilized instead of direct inversion in (6) to enhance computational efficiency, numerical stability, and memory usage.

III. EVALUATION

The performance of the MEC model is evaluated by comparing the torque and flux density predictions with the results from nonlinear FEA models developed in ANSYS Maxwell, a commercial FEA software. First, three diverse magnetic gear base designs presented in Table I and Fig. 7 were used for initial analyses. Additionally, an extensive parametric design optimization study investigated the MEC's capability to analyze and optimize a broad spectrum of design variations compared to FEA. These designs, along with the base designs, have the same geometries as those presented in [35] except that they have bridges. (As shown in Fig. 2, these bridges saturate heavily and require nonlinear analysis for accurate torque predictions.) The designs use M250 electrical steel for the ferromagnetic components and NdFeB N42 for the PMs.

A. Convergence Criterion

In this study, torque variation is used as the convergence criterion, as it is a key performance metric in MG optimization. The solution is considered converged when the torque variation between consecutive iterations falls below 0.1%, though this threshold can be adjusted to balance precision and computational speed. Fig. 8(a) shows the predicted torque values across iterations for three base designs, with results normalized

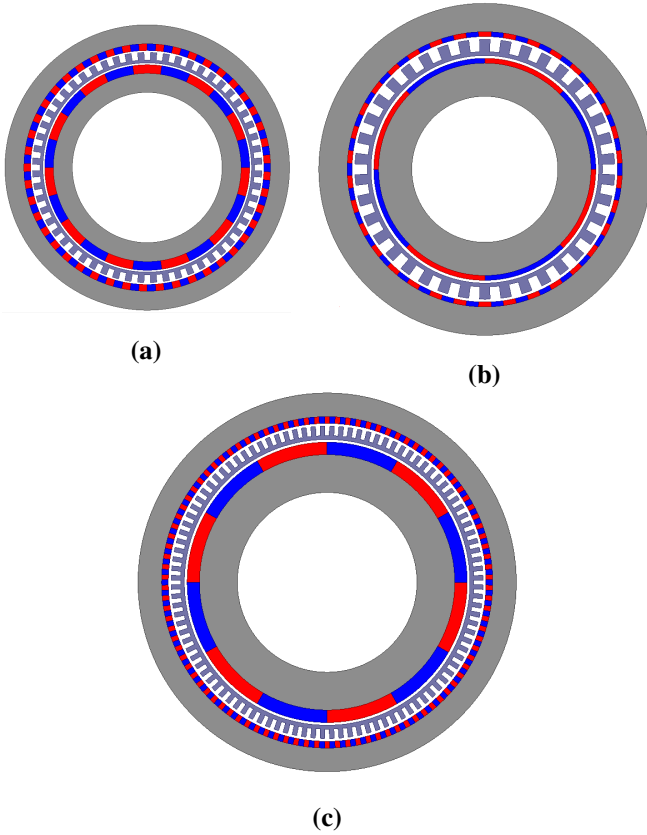


Fig. 7: Cross-sectional views of base designs (a) 1, (b) 2, and (c) 3. (Airgaps and bridges are enlarged for clarity.)

to the final solution. The predicted torque demonstrates rapid convergence for all three designs. Fig. 8(b) shows the RMS of the residual vector across iterations for three base designs. The Newton-Raphson algorithm effectively reduces the residual for each base design.

Fig. 8(c) illustrates the total simulation time after each iteration for each base design. The red circles indicate the iteration in which convergence was achieved. Each base design used the fine mesh discretization parameters from [35] to determine the number of radial and angular layers.

B. Initialization

The convergence of the Newton-Raphson method is highly sensitive to the choice of the initial guess [34]. Not all initial guesses will yield convergence, and, even for those that do, the number of iterations required will depend on the initial guess. Initial convergence tests demonstrated that using a relative permeability of 1 for ferromagnetic materials often resulted in the Newton-Raphson method failing to converge. However, using the solution of the linearized system 2 with an initial permeability value selected from the material's linear B-H region, such as 4000 for M250 electrical steel, generally yielded consistent convergence. This initialization approach was applied for the results shown in Fig. 8.

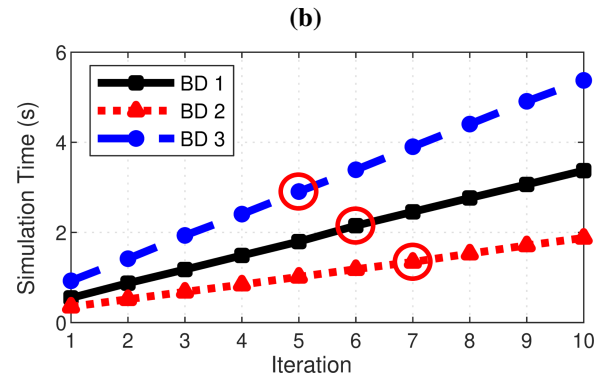
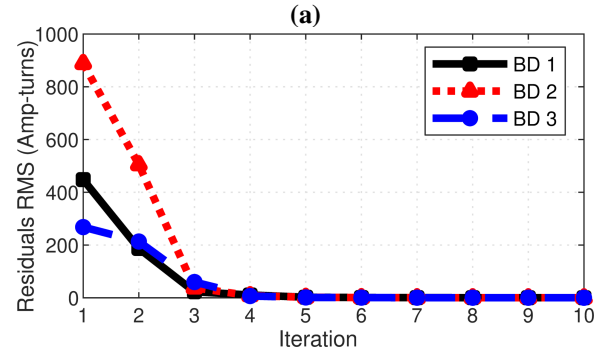
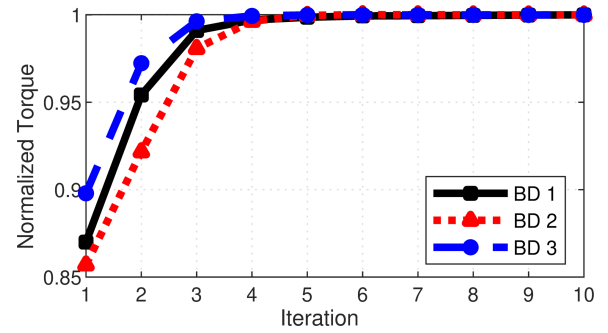


Fig. 8: For each of the base designs, comparison of (a) normalized torque, (b) RMS of the residual, and (c) total simulation time for different numbers of iterations.

C. Comparisons with FEA for Base Designs

The radial flux density distributions shown in Fig. 9 were calculated by the nonlinear FEA and MEC models along circular paths in the middle of the outer air gaps of the three base designs. The results indicate that the MEC produces highly accurate flux density distributions for these three designs.

The computational requirements for the base designs are compared in Table II for both analysis methods. The FEA model requires significantly more time to complete the analysis. However, the fine mesh MEC achieves comparable accuracy while reducing computational time by a factor of 16 to 38, while predicting the torque within 2.6% of the FEA for every case. Although the fine mesh MEC uses a larger number of elements, its simpler mathematical approach enables much faster computation than FEA's more complex electromagnetic field calculations. Using the coarse mesh settings described

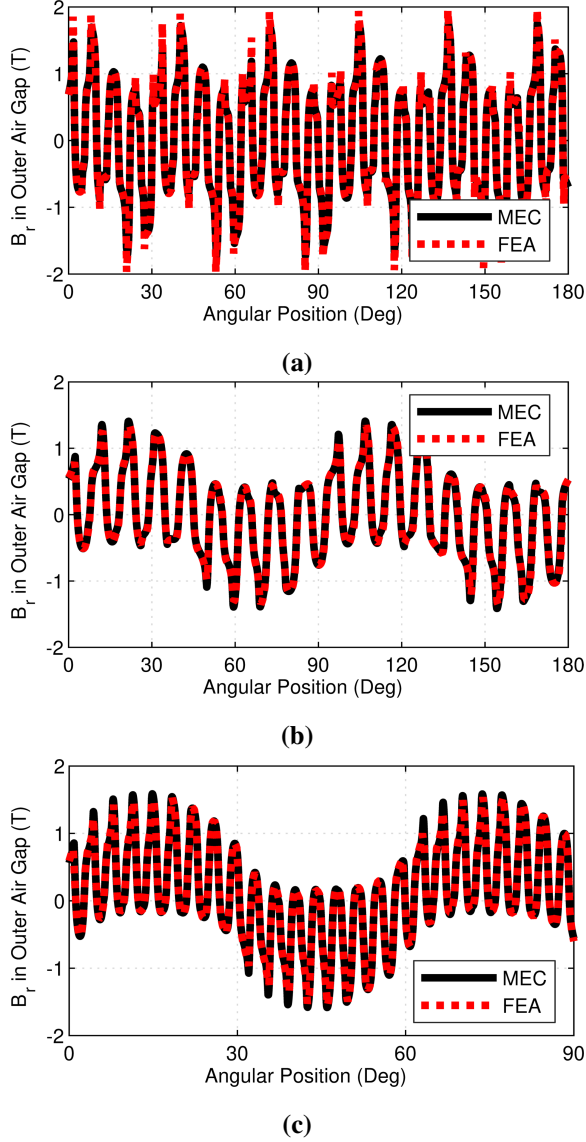


Fig. 9: Radial flux density along a circular path in the middle of the outer air gap of base designs (a) 1, (b) 2, and (c) 3.

TABLE II: Comparison of FEA and Fine Mesh MEC Analysis Details

Method	Metric	Base Design 1	Base Design 2	Base Design 3
FEA	Number of Elements	38,490	24,506	21,772
	Torque (kNm)	13.49	6.74	16.02
	Elapsed Time (sec)	69	44	48
Fine Mesh MEC	Number of Elements	228,480	127,680	611,520
	Torque (kNm)	13.37	6.62	15.61
	Elapsed Time (sec)	2.15	1.18	2.90
Coarse Mesh MEC	Number of Elements	45,920	26,600	114,400
	Torque (kNm)	13.06	6.40	15.19
	Elapsed Time (sec)	1.29	0.28	0.57

in [35] made the MEC 53 to 157 times faster than the FEA but increased the maximum discrepancy with the FEA's torque predictions to 5.2%.

D. Optimization Study

Previous research has demonstrated that mesh resolution significantly impacts both computational efficiency and model accuracy. [35]. While reduced layer counts can decrease computation time, they lead to less accurate slip torque predictions. To systematically assess this tradeoff and validate the effectiveness of the solution method, as well as the mesh settings and initialization strategy, an extensive parametric optimization study of RFMGs with bridges was performed. This comprehensive analysis served to evaluate the nonlinear MEC model's effectiveness as a rapid design tool. To do so, several critical gear parameters were swept over the ranges of values specified in Table III, and each of the resulting 140,000 designs was analyzed using the 2D nonlinear MEC model as well as a 2D nonlinear FEA model developed in ANSYS Maxwell. The MEC analysis was done using two different meshing resolutions, specified as the "coarse mesh" and "fine mesh" settings defined in Table IV, with the multipliers defined in [35]. Additionally, both coarse and fine mesh settings use two radial layers in the air regions inside the inner back iron and outside the outer back iron, where flux densities are expected to be relatively small. The bridge, being relatively thin is also divided into only two radial layers.

FEAs used in the optimization study were performed using ANSYS Maxwell's adaptive meshing with default settings in magnetostatic mode, which includes a percent error setting of 0.1%, a minimum of 3 passes, and a maximum of 20 passes.

TABLE III: Parameter sweep ranges for optimization study

Parameter	Description	Ranges of Values	Units
G_r	Integer part of gear ratio	5,9,17	
P_1	Inner pole pairs		
	For $G_r = 5$	4,5,6,...18	
	For $G_r = 9$	3,4,5,...13	
	For $G_r = 17$	3,4,5,...8	
r_O	Active outer radius	150, 175, 200	mm
k_{BI1}	Rotor 1 back iron thickness coefficient	0.4, 0.5, 0.6	
T_{PM1}	Rotor 1 PM thickness	3,5,7,...13	mm
T_{AG}	Air gap thickness (per gap)	1.5	mm
T_{Mods}	Rotor 2 thickness	11, 14, 17	mm
T_{BrG}	Bridge thickness	0.5, 1, 1.5	mm
k_{PM}	Rotor 3 PM thickness ratio	0.5, 0.75, 1	
T_{BI3}	Rotor 3 back iron thickness	20, 25, 30	mm

As in [35], to reflect the significant interactions between the various dimensions, some were coupled through derived coefficients included in Table III. The coefficient k_{PM} relates the radial thickness of the Rotor 3 PMs, T_{PM3} , to that of the Rotor 1 PMs, T_{PM1} , as expressed by

$$T_{PM3} = k_{PM} \times T_{PM1} \quad (7)$$

This approach is used because Rotor 3 has a higher PM pole count than Rotor 1, which results in increased flux leakage. Thus, the Rotor 3 PMs should not be thicker than the Rotor 1 PMs. Additionally, the coefficient, k_{BI1} , couples the radial thickness of the Rotor 1 back iron to the Rotor 1 pole arc to prevent excessive saturation, according to

$$T_{BI1} = k_{BI1} \left(\frac{\pi r_{BI1}}{P_1} \right) \quad (8)$$

TABLE IV: Magnetic Gear MEC Model Discretization Settings for the Optimization Study

Settings	Coarse Mesh	Fine Mesh
Angular layers multiplier	10	30
Radial layers in the rotor 1 back iron	3	3
Rotor 1 magnets radial layers multiplier	10	20
Inner air gap radial layers multiplier	10	20
Modulators radial layers multiplier	10	20
Outer air gap radial layers multiplier	10	20
Rotor 3 magnets radial layers multiplier	10	20
Radial layers in the rotor 3 back iron	3	3
Minimum radial layers in rotor 1 magnets	3	3
Minimum radial layers in inner air gap	3	3
Minimum radial layers in rotor 2	3	5
Minimum radial layers in outer air gap	3	3
Minimum radial layers in rotor 3 magnets	3	5

where r_{BI1} is the outer radius of the Rotor 1 back iron, as in [35]. Furthermore, G_r represents the integer part of the gear ratio and relates the pole pair counts according to

$$P_3 = \begin{cases} (G_{\text{int}} - 1)P_1 + 1, & G_{\text{int}}P_1 \text{ odd} \\ (G_{\text{int}} - 1)P_1 + 2, & G_{\text{int}}P_1 \text{ even} \end{cases} \quad (9)$$

This avoids integer gear ratios and designs lacking symmetry, which are prone to large torque ripples [2] and unbalanced magnetic forces on the rotors [30], respectively.

The graphs in Figs. 10-13 and the statistics in Table V compare the optimization study results obtained from the fine and coarse-meshed MEC with those from the FEA.

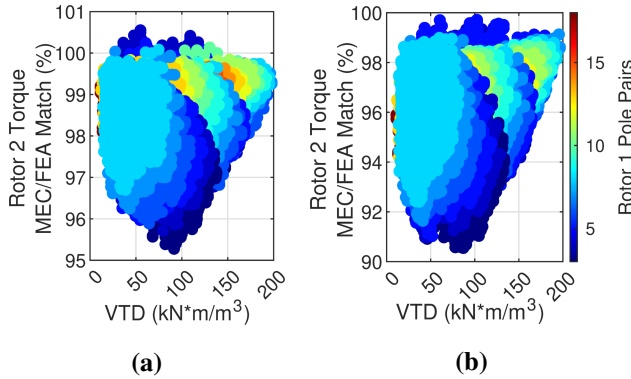


Fig. 10: MEC agreement with FEA over the full parametric sweep range with the (a) fine mesh and the (b) coarse mesh.

TABLE V: Summary of optimization study results

Metric	Fine Mesh MEC	Coarse Mesh MEC	FEA
Minimum Discrepancy	-4.7%	-9.45%	N/A
Maximum Discrepancy	0.55%	-0.29%	N/A
Average Absolute Discrepancy	1.54%	4.33%	N/A
Total Simulation Time (sec)	387,500	60,822	6,003,857
Average Simulation Time (sec)	2.77	0.43	42.89

Fig. 10 demonstrates the accuracy of the MEC models across the entire 140,000-design parametric sweep, indicating their fair accuracy over a wide range of volumetric torque densities (VTDs). Overall, the torque predictions from both

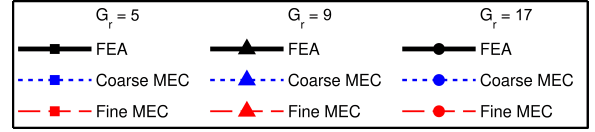


Fig. 11: Legend for design trend plots in Figs. 12 and 13

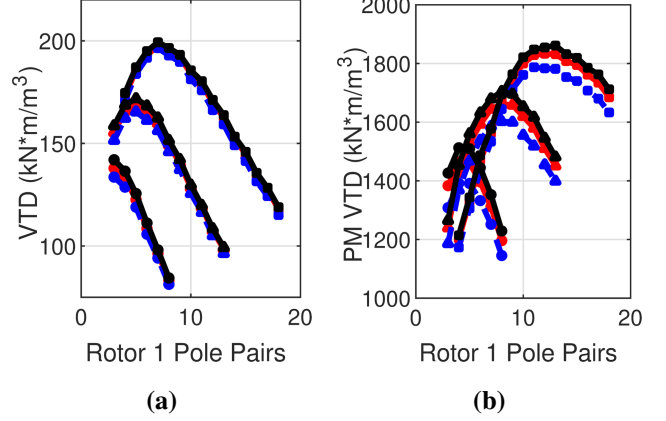


Fig. 12: Impact of Rotor 1 pole pair count on the maximum achievable (a) VTD and (b) PM VTD.

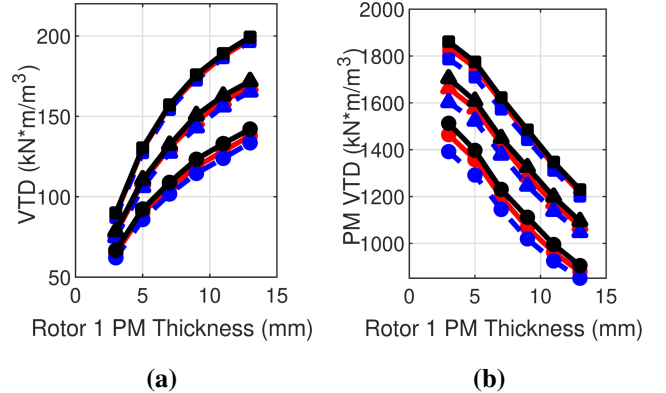


Fig. 13: Impact of Rotor 1 PM thickness on the maximum achievable (a) VTD and (b) PM VTD.

fine and coarse mesh MEC models closely correspond to those from FEA models, with discrepancies less than 5% and 10%, respectively. Notably, the MEC models exhibit closer agreement with the FEA for designs with higher VTDs, indicating that the accuracy is best for the designs most likely to be of interest. Specifically, for the designs with the top 10% of VTDs, the maximum absolute discrepancies are 2% and 4.5% for fine and coarse mesh MEC models, respectively. Figs. 12 and 13 indicate the MEC model's accurate tracking of key performance trends, particularly in VTD and PM VTD (defined as slip torque divided by PM material volume) relative to the Rotor 1 pole pair count and PM thickness. Table V presents a statistical analysis demonstrating the accuracy and speed of the coarse and fine mesh MEC models compared to the FEA model across the entire parametric design space outlined in Table III. On average, the fine and coarse mesh MEC models are about 15 and 100 times as fast as the FEA, respectively.

All FEA and MEC simulations in this paper were performed on workstations equipped with an 8-core Intel® Core™ i7-10700K processor (3.80GHz) and 64GB RAM.

IV. CONCLUSION

This study has developed a fast, robust, and adaptive 2D nonlinear MEC model for radial flux magnetic gears with bridges. The model can accurately predict torque and air gap flux densities for a wide range of RFMG designs with highly saturated bridges significantly faster than 2D FEA. The systematic approach parametrically discretizes the RFMG into mesh loops and applies mesh-flux analysis to each mesh loop to construct the reluctance matrix. Because the reluctance matrix is a function of mesh fluxes, the resulting system of equations is nonlinear. The Newton-Raphson iterative method provides a fast and reliable solution to this nonlinear system.

The systematic initialization strategy ensures fast and accurate convergence. The nonlinear MEC demonstrates excellent agreement with FEA on the air gap flux densities for three diverse base designs with bridges. An extensive optimization study comprising 140,000 designs validates that the nonlinear MEC consistently aligns with FEA torque predictions and accurately tracks design trends.

The results demonstrate that the presented model achieves 15 to 100 times faster analysis while maintaining average discrepancies of only 1.54% and 4.5% relative to the FEA model's torque predictions for the fine and coarse meshed MECs, respectively. These findings establish the proposed model as an efficient and reliable tool for the rapid design optimization of magnetic gears with bridges.

2D analysis methods, despite their tendency to overpredict performance due to end effects [31], remain valuable in magnetic gear design. Their primary advantage is computational efficiency compared to 3D methods, making them practical for parametric sweeps and early-stage optimization. While 3D analysis is essential for final validation, 2D methods can effectively identify design trends and optimize parameters such as pole counts and magnet thicknesses at a significantly lower computational cost [28], [41]. Furthermore, by accounting for end effects and aspect ratios, 2D results can be adjusted to provide reasonable performance estimates, reinforcing their importance as essential early-stage design tools [4]. Future work would include extending this model to 3D so that it is suitable for final validation of magnetic gear designs.

REFERENCES

- [1] G. Tao *et al.*, "Experimental comparison of acoustic characteristics for a high-efficiency magnetic gearbox and a mechanical planetary gearbox for industrial hvac applications," *IEEE Trans. Energy Convers.*, vol. 39, no. 1, pp. 182–190, 2024.
- [2] N. W. Frank and H. A. Toliyat, "Gearing ratios of a magnetic gear for wind turbines," in *Proc. IEEE Int. Electr. Mach. Drives Conf.*, 2009, pp. 1224–1230.
- [3] K. Li *et al.*, "Designing and experimentally testing a magnetic gearbox for a wind turbine demonstrator," *IEEE Trans. Ind. Appl.*, vol. 55, pp. 3522–3533, July 2019.
- [4] A. B. Kjaer, S. Korsgaard, S. S. Nielsen, L. Demsa, and P. O. Rasmussen, "Design, fabrication, test, and benchmark of a magnetically geared permanent magnet generator for wind power generation," *IEEE Trans. Energy Convers.*, vol. 35, pp. 24–32, Mar. 2020.
- [5] K. K. Uppalapati, J. Z. Bird, D. Jia, J. Garner, and A. Zhou, "Performance of a magnetic gear using ferrite magnets for low speed ocean power generation," in *Proc. IEEE Energy Convers. Congr. Expo.*, 2012, pp. 3348–3355.
- [6] P. O. Rasmussen, T. V. Frandsen, K. K. Jensen, and K. Jessen, "Experimental evaluation of a motor-integrated permanent-magnet gear," *IEEE Trans. Ind. Appl.*, vol. 49, no. 2, pp. 850–859, 2013.
- [7] T. V. Frandsen, P. O. Rasmussen, and K. K. Jensen, "Improved motor integrated permanent magnet gear for traction applications," in *Proc. IEEE Energy Convers. Congr. Expo.*, 2012, pp. 3332–3339.
- [8] T. V. Frandsen *et al.*, "Motor integrated permanent magnet gear in a battery electrical vehicle," *IEEE Trans. Ind. Appl.*, vol. 51, no. 2, pp. 1516–1525, 2015.
- [9] P. Chmelicek, S. D. Calverley, R. S. Dragan, and K. Atallah, "Dual rotor magnetically geared power split device for hybrid electric vehicles," *IEEE Trans. Ind. Appl.*, vol. 55, no. 2, pp. 1484–1494, 2019.
- [10] P. O. Rasmussen, H. H. Mortensen, T. N. Matzen, T. M. Jahns, and H. A. Toliyat, "Motor integrated permanent magnet gear with a wide torque-speed range," in *Proc. IEEE Energy Convers. Congr. Expo.*, 2009, pp. 1510–1518.
- [11] T. F. Talerico, Z. A. Cameron, J. J. Scheidler, and H. Hasseeb, "Outer stator magnetically-geared motors for electrified urban air mobility vehicles," in *Proc. AIAA/IEEE Electr. Aircr. Technol. Symp.*, 2020, pp. 1–25.
- [12] R. S. Dragan, R. E. Clark, E. K. Hussain, K. Atallah, and M. Odavic, "Magnetically geared pseudo direct drive for safety critical applications," *IEEE Trans. Ind. Appl.*, vol. 55, no. 2, pp. 1239–1249, 2019.
- [13] G. Puchhammer, "Magnetic gearing versus conventional gearing in actuators for aerospace applications," in *Proc. Aero. Mech. Symp.*, 2014, pp. 175–181.
- [14] V. M. Asnani, J. J. Scheidler, and T. F. Talerico, "Magnetic gearing research at nasa," in *Proc. AHS Int. Annu. Forum*, 2018, pp. 1–14.
- [15] J. J. Scheidler, V. M. Asnani, and T. F. Talerico, "Nasa's magnetic gearing research for electrified aircraft propulsion," in *Proc. AIAA/IEEE Electr. Aircr. Technol. Symp.*, 2018, pp. 1–12.
- [16] J. J. Scheidler, Z. A. Cameron, and T. F. Talerico, "Dynamic testing of a high-specific-torque concentric magnetic gear," in *Proc. Vertical Flight Soc. Annu. Forum*, 2019, pp. 1–8.
- [17] T. F. Talerico, Z. A. Cameron, J. J. Scheidler, and H. Hasseeb, "Outer stator magnetically-geared motors for electrified urban air mobility vehicles," in *Proc. AIAA/IEEE Electr. Aircr. Technol. Symp.*, 2020, pp. 1–25.
- [18] B. Praslicka, M. C. Gardner, M. Johnson, and H. A. Toliyat, "Review and analysis of coaxial magnetic gear pole pair count selection effects," *IEEE J. Emerg. Sel. Top. Power Electron.*, vol. 10, no. 2, pp. 1813–1822, 2022.
- [19] B. Praslicka *et al.*, "Design and analysis of an axial flux coaxial magnetic gear with balanced axial forces for precision aerospace actuation application," in *Proc. IEEE Energy Convers. Congr. Expo.*, 2022, pp. 1–8.
- [20] H. Y. Wong, H. Baninajar, B. W. Dechant, P. Southwick, and J. Z. Bird, "Experimentally testing a halbach rotor coaxial magnetic gear with 279 nm/l torque density," *IEEE Trans. Energy Convers.*, vol. 38, no. 1, pp. 507–518, 2023.
- [21] M. Johnson, M. C. Gardner, and H. A. Toliyat, "A parameterized linear magnetic equivalent circuit for analysis and design of radial flux magnetic gears—part i: Implementation," *IEEE Trans. Energy Convers.*, vol. 33, pp. 784–791, June 2018.
- [22] X. Ran, J. Shang, M. Zhao, and Z. Yi, "Improved configuration proposal for axial reluctance resolver using 3-d magnetic equivalent circuit model and winding function approach," *IEEE Trans. Transp. Electr.*, vol. 9, no. 1, pp. 311–321, 2023.
- [23] G. Vidanalage, B. D. Silva, A. Lombardi, J. Tjong, and N. C. Kar, "Magnetic field-based induction machine modeling incorporating space and time harmonic effects," *IEEE Access*, vol. 12, pp. 41 579–41 589, 2024.
- [24] P. Wu and Y. Sun, "A hybrid model for calculating on-load performance of delta-type ipm machines accounting for rotor and stator saturation," *IEEE Trans. Ind. Electron.*, pp. 1–11, 2024.
- [25] R. Benlamine, T. Hamiti, F. Vangraefscheppe, F. Dubas, and D. Lhotellier, "Modeling of a coaxial magnetic gear equipped with surface mounted pms using nonlinear adaptive magnetic equivalent circuits," in *Proc. IEEE Int. Conf. Elect. Mach.*, 2016, pp. 1888–1894.
- [26] M. Fukuoka, K. Nakamura, and O. Ichinokura, "Dynamic analysis of planetary-type magnetic gear based on reluctance network analysis," *IEEE Trans. Magn.*, vol. 47, no. 10, pp. 2414–2417, 2011.

- [27] S. A. Khan, G. Duan, and M. C. Gardner, "Comparison of modulator retention shapes for radial flux coaxial magnetic gears," in *Proc. IEEE Energy Convers. Congr. Expo.*, 2022, pp. 1–7.
- [28] M. Johnson *et al.*, "Design, construction, and analysis of a large-scale inner stator radial flux magnetically geared generator for wave energy conversion," *IEEE Trans. Ind. Appl.*, vol. 54, no. 4, pp. 3305–3314, 2018.
- [29] H. Baninajar *et al.*, "Designing a halbach rotor magnetic gear for a marine hydrokinetic generator," *IEEE Trans. Ind. Appl.*, vol. 58, no. 5, pp. 6069–6080, 2022.
- [30] G. Jungmayr, J. Loeffler, B. Winter, F. Jeske, and W. Amrhein, "Magnetic gear: Radial force, cogging torque, skewing and optimization," in *Proc. IEEE Energy Convers. Congr. Expo.*, 2015, pp. 898–905.
- [31] S. Gerber and R.-J. Wang, "Analysis of the end-effects in magnetic gears and magnetically geared machines," in *Proc. Int. Conf. Electr. Mach.*, 2014, pp. 396–402.
- [32] S.-H. Lee, S.-Y. Im, J.-Y. Ryu, and M.-S. Lim, "Optimum design process of coaxial magnetic gear using 3d performance prediction method considering axial flux leakage," *IEEE Trans. Ind. Appl.*, vol. 60, no. 2, pp. 3075–3085, 2024.
- [33] H. Diab, Y. Amara, and G. Barakat, "A 3d nonlinear magnetic equivalent circuit model for an axial field flux focusing magnetic gear: Comparison of fixed-point and newton–raphson methods," *Mathematics and Computers in Simulation*, vol. 224, pp. 119–137, 2024.
- [34] S. C. Chapra and R. P. Canale, *Numerical Methods for Engineers.*, 7th ed. McGraw Hill, 2015.
- [35] M. Johnson, M. C. Gardner, and H. A. Toliyat, "A parameterized linear magnetic equivalent circuit for analysis and design of radial flux magnetic gears—part ii: Evaluation," *IEEE Trans. Energy Convers.*, vol. 33, pp. 792–800, June 2018.
- [36] B. Boomiraja and R. Kanagaraj, "Convergence behaviour of newton–raphson method in node- and loop-based non-linear magnetic equivalent circuit analysis," in *Proc. IEEE Int. Conf. Power Electron. Smart Grid Renew. Energy*, 2020, pp. 1–6.
- [37] A. Hemeida, A. Lehtikoinen, P. Rasilo, H. Vansompel, A. Belahcen, A. Arkkio, and P. Sergeant, "A simple and efficient quasi-3d magnetic equivalent circuit for surface axial flux permanent magnet synchronous machines," *IEEE Trans. Ind. Electron.*, vol. 66, no. 11, pp. 8318–8333, 2019.
- [38] D. C. Horvath, S. D. Pekarek, and S. D. Sudhoff, "A scaled mesh/nodal formulation of magnetic equivalent circuits with motion," *IEEE Trans. Energy Convers.*, vol. 34, no. 1, pp. 58–69, 2019.
- [39] R. Wang, S. Pekarek, M. L. Bash, A. Larson, and R. V. Maaren, "Incorporating dynamics in a mesh-based magnetic equivalent circuit model of synchronous machines," *IEEE Trans. Energy Convers.*, vol. 30, no. 3, pp. 821–832, 2015.
- [40] T. A. Davis, "Algorithm 930: Factorize: An object-oriented linear system solver for matlab," *ACM Trans. Math. Softw.*, vol. 39, no. 4, pp. 1–18, Jul. 2013.
- [41] M. Johnson, M. C. Gardner, and H. A. Toliyat, "Design comparison of ndfeb and ferrite radial flux surface permanent magnet coaxial magnetic gears," *IEEE Trans. Ind. Appl.*, vol. 54, no. 2, pp. 1254–1263, 2018.

Danial Kazemikia earned his B.Sc. degree in electrical engineering from K. N. Toosi University, Tehran, Iran in 2019. He is currently a Ph.D. student in electrical engineering at the University of Texas at Dallas. His research interests are computational electromagnetics, design optimization, and physics-informed neural networks focusing on the design and control of electric machines and magnetic gears.

Matthew C. Gardner earned his B.S. in electrical engineering from Baylor University, Waco, Texas in 2014. He earned his Ph.D. in electrical engineering from Texas A&M University, College Station, Texas in 2019. In August 2020, he joined the University of Texas at Dallas, where he is an assistant professor. His research interests include optimal design and control of electric machines and magnetic gears.